



HAL
open science

Characterisation of boundary layer transition over a low Reynolds number rotor

Thomas Jaroslowski, Maxime Forte, Jean-Marc Moschetta, Gregory Delattre,
Erwin Ricky Gowree

► **To cite this version:**

Thomas Jaroslowski, Maxime Forte, Jean-Marc Moschetta, Gregory Delattre, Erwin Ricky Gowree. Characterisation of boundary layer transition over a low Reynolds number rotor. *Experimental Thermal and Fluid Science*, 2022, 130, pp.110485. 10.1016/j.expthermflusci.2021.110485 . hal-03340224

HAL Id: hal-03340224

<https://hal.science/hal-03340224>

Submitted on 10 Sep 2021

HAL is a multi-disciplinary open access archive for the deposit and dissemination of scientific research documents, whether they are published or not. The documents may come from teaching and research institutions in France or abroad, or from public or private research centers.

L'archive ouverte pluridisciplinaire **HAL**, est destinée au dépôt et à la diffusion de documents scientifiques de niveau recherche, publiés ou non, émanant des établissements d'enseignement et de recherche français ou étrangers, des laboratoires publics ou privés.



Open Archive Toulouse Archive Ouverte (OATAO)

OATAO is an open access repository that collects the work of some Toulouse researchers and makes it freely available over the web where possible.

This is an author's version published in: <https://oatao.univ-toulouse.fr/28178>

Official URL : <https://doi.org/10.1016/j.expthermflusci.2021.110485>

To cite this version :

Jaroslawski, Thomas and Forte, Maxime and Moschetta, Jean-Marc and Delattre, Gregory and Gowree, Erwin Ricky Characterisation of boundary layer transition over a low Reynolds number rotor. (2022) Experimental Thermal and Fluid Science, 130. 110485. ISSN 0894-1777

Any correspondence concerning this service should be sent to the repository administrator:

tech-oatao@listes-diff.inp-toulouse.fr

Characterisation of boundary layer transition over a low Reynolds number rotor

Thomas Jaroslowski^{a,*}, Maxime Forte^a, Jean-Marc Moschetta^b, Gregory Delattre^a, Erwin R. Gowree^b

^a ONERA, DMPE, Université de Toulouse, 31055 Toulouse, France

^b ISAE-SUPAERO, Université de Toulouse, 31055 Toulouse, France

A B S T R A C T

Keywords:

Infrared Thermography
Boundary layer transition
Low Reynolds number
Rotor

An experimental investigation on the flow topology over a rotor operating at low Reynolds numbers is presented. The feasibility of laminar to turbulent transition experiments over small rotors is demonstrated. Phase-locked infrared thermography coupled with simultaneous force and torque measurements were used to study a three bladed rotor with a NACA0012 aerofoil section set at a uniform angle of incidence of 10° . Boundary layer transition was forced using two-dimensional (2D) and three-dimensional (3D) roughness elements, placed at approximately 5% and 28% of the rotor blades chord. In the 3D roughness configurations once the critical roughness Reynolds was attained the streaks downstream developed into fully turbulent wedges. For the current rotor configuration, it was found that the state of the boundary layer can significantly affect its performance, with the non-optimal forcing of laminar to turbulent transition generally resulting in a loss of performance when compared to the smooth reference rotor case.

1. Introduction

Further knowledge of low Reynolds number flows is becoming increasingly important due to the rise in the demand of micro-aerial vehicles (MAV). This encourages us to rethink the way conventional aerodynamic design is conducted, as these vehicles operate within a Reynolds number ($Re = U_{tip}c/\nu$, where c denotes, ν the kinematic viscosity and for a rotor blade: $U_{tip} = R\Omega$, where R is the blade radius and Ω is the rotational speed.) regime of $10^3 < Re < 10^5$ where one can expect that the flow remains laminar to a greater extent but is still susceptible to transition. With MAV systems projected to operate in highly turbulent environments [1,2], understanding the impact of boundary layer transition becomes critical for the design of low Reynolds number flyers as it could lead to considerable deterioration in performance or in worst case scenarios, massive stall and control loss as they are more prone to separation in the low Reynolds number regime. An adverse pressure gradient over an aerofoil can cause formation of a laminar separation bubble (LSB), which at low and moderate angles of attack can undergo transition and reattach into a turbulent boundary layer. Though at high incidence it would break down into a long bubble without reattaching and cause laminar stall. In the turbulent state, the flow is more resilient

to separation at the cost of higher skin friction drag which compromises the endurance of the vehicle. Therefore, the location of boundary layer transition becomes a critical parameter during the design and optimisation of low Reynolds number aerodynamic surfaces.

For 2D boundary layers subjected to a low disturbance environment, laminar to turbulent transition occurs through the exponential growth of Tollmien-Schlichting (TS) waves. An adverse pressure gradient will promote more rapid growth, reducing the local Reynolds number at which transition occurs. At low Reynolds numbers ($< 10^5$) an LSB will be promoted in this recovery or adverse pressure gradient region, significantly modifying the pressure distribution of the aerofoil. Environmental perturbations can be convected within the separation bubble and grow very rapidly leading to transition of the detached shear layer and reattachment [3–7]. Turbulent reattachment will generally not occur for aerofoils with chord Reynolds numbers less than 7×10^4 , resulting in breakdown into a long bubble [3,8]. However, as the Reynolds number is increased, the length of the LSB decreases and reattachment is usually possible [9]. Therefore, the impact on the pressure distribution over the aerofoil is less significant resulting in little performance loss. These are semi-empirical observations which can be very useful for design and optimisation of low Reynolds number aerofoils,

* Corresponding author.

E-mail address: thomas.jaroslowski@onera.fr (T. Jaroslowski).

however the stability and dynamics are much more complicated.

Flow separation is an important factor in low Reynolds number aerofoil design philosophy, while trying to extend the amount of laminar flow and delaying transition to turbulence when skin friction drag reduction is necessary. As mentioned above, the impact of the LSB and laminar separation on the performance of a 2D low Reynolds number aerofoil is well studied, however less is understood on how external perturbations such as roughness or freestream turbulence impact these mechanisms. Furthermore, for low Reynolds number rotors, there are significantly fewer studies. Singh and Ahmed [10] took the LSB into consideration when designing a low Reynolds number wind turbine and noted that separation bubbles over low Reynolds number rotors cause excessive pressure drag, loss in aerodynamic lift and increase in the noise produced by the rotor. A recent study, on a rotor blade similar to that of the NASA Mars helicopter, by Argus et al. [11], used mid-fidelity RANS simulations coupled with a Blade Element Momentum Theory model to find that at $Re = 2 \times 10^4$ and 8×10^4 increasing the critical N-factor (the amount of perturbation growth required for transition) from 3 to 11 decreased the figure of merit (FM) of the rotor by approximately 40% suggesting that a performance gain is possible. They noted that in their configuration laminar separation without reattachment was the transition mechanism that deteriorated performance.

Infrared Thermography (IRT) is a common technique [12,13] used to detect the location of laminar to turbulent transition, over fixed and rotary aerofoils. The heat transfer between the blade surface and the flow in a turbulent boundary layer is larger than that in a laminar boundary layer, therefore it is possible to determine where the flow transitions from a laminar to turbulent state by comparing the heat transfer rate. If the surface is colder than the freestream flow then it will experience rapid heating, for instance in high speed flow. However, if the surface is hotter, then it will experience a cooling effect instead, due to the higher entrainment from a turbulent flow. Adiabatic recovery temperatures are lower in laminar flows than in turbulent flows, however in subsonic flows the resulting temperature differences are too low for reliable IR measurements. To address this problem, external or internal heating is used to increase the temperature gradient between the flow and the surface to account for the sensitivity and increase the accuracy in the measurement.

This method has been successfully used in a vast number of IR thermography on fixed and rotary wing transition experiments, for example, Horstmann et al. [14] used IR thermography during wind tunnel and in flight tests to successfully identify the position of laminar to turbulent transition over a wing glove, Dollinger et al. [15] demonstrated that IRT could be used to study boundary transition on full-scale wind turbines and Seraudie et al. [16] investigated the effects of Reynolds number on the transition mechanisms over a high lift swept wing, showing that the transition position and mechanism change with the Reynolds number. Raffel et al. [17] used differential infrared thermography (DIT) measurements for unsteady transition measurements. Using differential images with a small temporal separation (200 ms) they were able to identify the beginning and end of transition. They used the spatially averaged pixel intensity as a marker, suggesting that a steep drop in intensity corresponded to the onset of transition. DIT was also used by Weiss et al. [18] to measure the transition position on a rotating blade under cyclic pitch conditions. Miozzi et al. [19] investigated an LSB ($Re = 8 \times 10^4$) over a NACA 0015 aerofoil and were able to characterize a coherent structure from time-resolved IR temperature measurements. They found that separation and reattachment locations corresponded to the locations of local maximum and minimum surface temperature, respectively. They stated that inside the laminar separation bubble the transition point corresponded to the maximum chordwise temperature gradient. Wynnychuk and Yarusevych [20] investigated an LSB (for $Re = 8 \times 10^4$ and 1.2×10^5) over a NACA 0018 aerofoil using IRT and Particle Image Velocimetry (PIV), they found that the location of mean turbulent reattachment corresponded with the

location of minimum surface temperature.

Experimental investigations on boundary layer transition for rotor blades are relatively scarce. Maldonado and Gupta [21] studied the impact of piezoelectric-based synthetic jet actuators on the boundary layer development over a 3 bladed rotor (S809 aerofoil, $Re = 1.8 \times 10^5$) using Laser-Doppler Velocity (LDV) measurements. Contemporary boundary layer transition research on rotors most commonly uses IR thermography, where investigations on laminar to turbulent transition in rotary wing configurations entail more experimental difficulties than in fixed wing configurations. Richter and Schülein [22] used high-speed IRT for boundary layer transition measurements on the suction side of a helicopter rotor. By synchronizing the IR camera with the rotor they were able to identify the start and end of transition by tracing the evolution of the pixel intensity for the entire rotor blade from a single IR image. Lang et al. [23] used IRT and PIV to detect the presence of an LSB over a NACA 0015 rotor blade, showing that, the elevated temperature region could be used to determine the location of the bubble, the local Re where the bubble was measured was 1.4×10^5 . The locations of laminar separation and turbulent reattachment were approximated through the analysis of the chordwise pixel intensity gradient. They defined the mean transition location as the mid-point between the location of laminar separation and turbulent reattachment. Recently, Thiessen and Shülein [24] conducted transition experiments over a low Reynolds number quadcopter rotor using IRT and oil film topography measurements. They found a region of separated flow, which they claimed to be an LSB that forms over the rotor blade. The laminar separation bubble is a zone of almost stationary or low speed reverse flow, where the shear stress is zero or very low. In the separation region the heat transfer will be minimal and will begin to increase rapidly as transition and turbulent reattachment take place. In general, IR measurements conducted on a model which has a higher surface temperature than the free stream allows for identification of turbulent regions (low temperature), separated regions (high temperature) and laminar regions (medium temperature regions).

There exists a significant knowledge gap on the experimental study of boundary layer transition for rotors operating at the Reynolds number range applicable to UAV. The objective of the present study is to address this, by using IR thermography coupled with force/torque measurements to demonstrate the feasibility of the experimental study of boundary layer transition over small rotors at low Reynolds numbers. The flow topology of the smooth rotor is investigated, along with the impact of 2D and 3D roughness and their chordwise position on the state of the boundary layer and the flow topology over the rotor.

2. Methods

2.1. Experimental Setup

When experimentally or numerically investigating the aerodynamics of rotor blades, there is a trade-off between two setups: (1) a highly optimized rotor, where the aerodynamics are closer to "realistic" conditions, with the drawback being that these sorts of configurations are very case specific and the behaviour of the flow is difficult to interpret, and (2) testing a more generic rotor blade with less variables, where the physics can be more straightforward to understand, with the drawback of being less representative of application. The process of laminar to turbulent transition over low Reynolds number rotors is too poorly understood to be investigated over a complex optimized rotor. Therefore, the present investigation will be on a simple rotor operating over a Reynolds number range that is applicable to MAV.

The experiments were conducted at the Institut Supérieur de l'Aéronautique et de l'Espace (ISAE-SUPAERO) with the collaboration of ONERA in Toulouse, France. The experimental set up is presented in Fig. 1a and the rotor model with the roughness configurations are presented in Fig. 1b. The rotor had three blades with a NACA0012 profile,

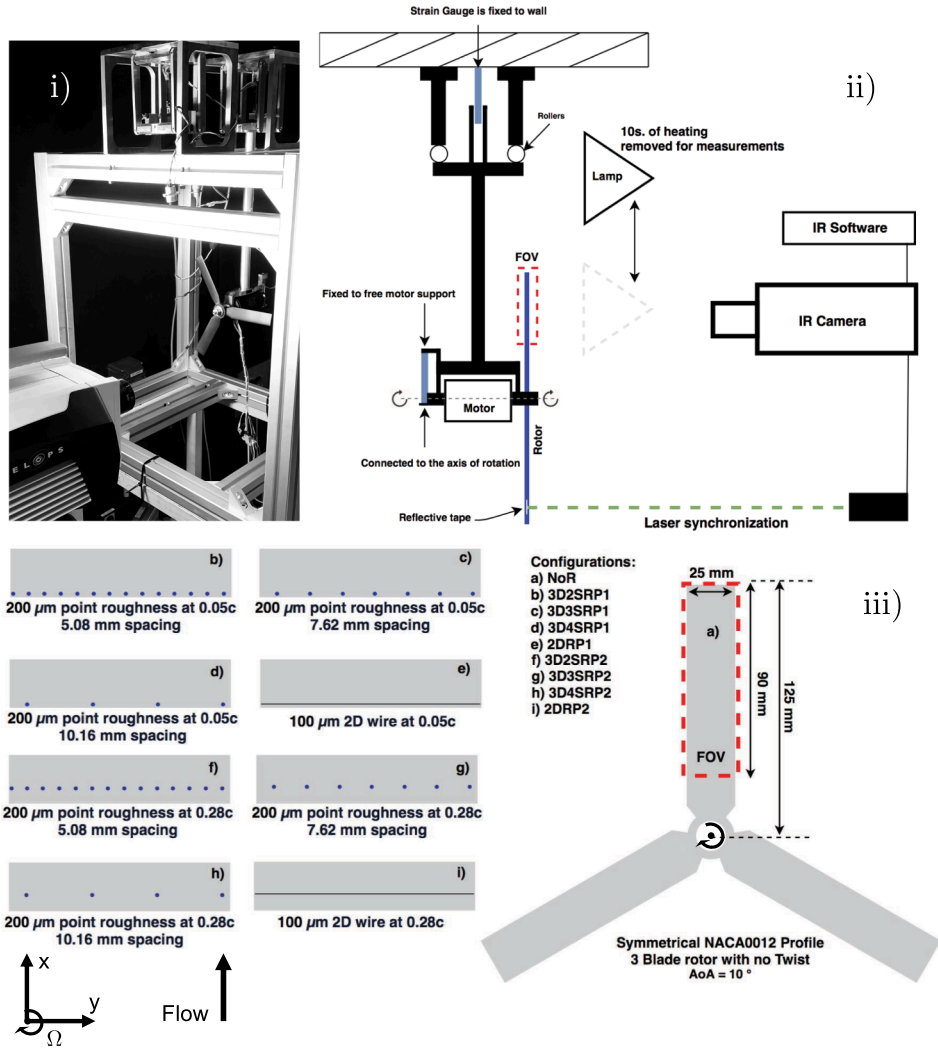


Fig. 1. i) Low Reynolds number rotor test rig; Schematic of the experimental setup; iii) Roughness configurations (blue marks and black lines denote 3D isolated roughness element and 2D wire, respectively). (For interpretation of the references to colour in this figure legend, the reader is referred to the web version of this article.)

an angle of incidence of 10° and no twist. The radius (R) of the rotor was 0.125 m and the chord length (c) was 0.025 m, resulting in the rotor having an aspect ratio ($AR = R/c$) of 5. The rotor blades were 3D printed using a reinforced resin, great care was taken to ensure that the blade was smooth. Phase locked IRT was used to capture the temperature distribution of the rotor blade's surface. A Brüel kJær CCLD laser tachometer was used to synchronize the blade with the IR camera. A thin reflective film was placed on an opposing blade, so that for each rotation a voltage pulse was sent out by the laser to trigger the camera. In order to increase the temperature difference between the ambient air and the blades surface, a 500 W halogen lamp was used to increase the surface temperature of the blade of interest.

A schematic of the experimental configuration can be found in Fig. 1., the rotor was operated in hover in a very large room with respect to the rotor dimensions, in static air the freestream turbulence can be assumed to be negligible. Before starting the measurement, the blade of interest was systematically heated by the lamp at a distance of 0.15 m for 10 s. The room temperature was at 20°C and the blade was heated to approximately $35\text{--}40^\circ\text{C}$ in each case, however the absolute temperature is not of great importance as the transition detection techniques are based on temperature differences. Energy injected into the flow due to heating of the blade can affect the critical Reynolds number at which boundary layer transition occurs [25], however this is mainly relevant

for modal transition which is bypassed when transition occurs immediately downstream of a 3D roughness. Furthermore, the heating is too low to affect the transition process, especially at the low Reynolds numbers studied, where the boundary layer is much more stable. In previous work, the overheat temperature employed was between $10\text{--}20^\circ\text{C}$, where [17,19,20] suggested that these levels of overheat do not significantly affect transition position. Furthermore, The Richardson number can be used to address the extent of the relevance of natural convection to forced convection. The Richardson number is defined in Eq. 1, where θ , represents the volumetric thermal expansion coefficient ($105 \times 10^{-6}/^\circ\text{C}$), the rotational acceleration is defined as $a = \Omega_{tip}^2/r$ and used instead of the acceleration due to gravity as rotational accelerations would dominate. The surface temperature of the the model and the ambient air temperature are denoted by T_w and T_∞ , respectively.

$$Ri = c\theta(T_w - T_\infty)/r \quad (1)$$

Natural convection can be considered to be negligible if $Ri < 0.1$, in the present work $Ri \sim 0.0032$ at $r/R = 0.1$ and decreases as r/R is increased, therefore natural convection effects on the flow can be neglected. During the IR camera measurement the heating lamp was turned off, the motivation of this technique is that in a turbulent flow region there will be more heat transfer between the blade surface and outer flow than in a laminar flow region. Therefore the temperature

(pixel intensity) will vary in a turbulent, laminar or separated region as a function of time. Since a variety of configurations were tested, a pixel intensity normalization technique needed to be implemented for coherent analysis. Each IR image was normalized by the maximum pixel intensity present in the image so that the different test configurations would be compared reliably. The high speed and high resolution IR camera (Telops Fast M3k) was used to characterize the flow topology over the rotor, where the pixel intensity is used to approximate the state of the boundary layer. The camera had 320 x 256 pixel spatial resolution, a typical NETD of 25 mK and operated in the 1.5–5.4 μ m spectral range and was positioned 0.4 m away from the rotor blade. The size of the field of view was 1c x 0.65R and the exposure time of the camera was 71 μ s, allowing for a good compromise between camera noise and motion blur. Since the camera was synchronized with the rotor, effectively, the sampling rate was that of the rotors turning rate (RPM) for the given run. Motion blur is one of the greatest challenges when conducting IR measurements, even with state-of-the-art cameras. To mitigate this, at least 500 phase locked images were captured for each run. The Motion blur can be calculated by multiplying the exposure time of the camera by the local radial velocity. Increasing the rotational speed and radial position results in more blur. For example at the highest speed, 6500 RPM and at the blade tip, the motion blur can be up to 0.24c, however this value is less than 0.1c for a large portion of the blade as the radial velocity decreases moving inboard. When raw images were analyzed the blur was not significant enough to affect the test result potentially due to the reliable synchronisation. Furthermore, at lower rotational speeds, the blur is between 0.01c and 0.1c, depending on speed and radial position. The test matrix is presented in Table 1.

Referring to Figs. 1i and ii, the thrust and torque were measured using the same aerodynamic balance as in Desert et al. [26]. The aerodynamic balance used load cells to measure the thrust and torque. To measure the thrust, one end of the load cell was fixed to the motor driving the rotor and the other to a fixed support. The torque is measured by fixing one end of the load cell to a circular plate fixed to the back of the motor (aligned with the axis of rotation) and the other to a fixed frame surrounding the motor. The frame allows for free rotation of the motor along its axis through two ball bearings. Therefore when a torque is applied, it pushes onto the load cell. It must be noted, that the experimental setup measured the sum of the aerodynamic torque exerted by the rotor on the motor and the internal mechanical torque of the motor. The sampling frequency of the force and torque measurements was 500 Hz, 5000 samples were acquired, with a 10 s stabilization period between each speed interval. The force and torque were measured for long enough so that their means and standard deviations converged. The uncertainty of the thrust and torque measurements was calculated using a 95% confidence interval, the total uncertainty for the thrust and torque was approximately 1% and 0.045 % of full scale, respectively.

Referring to the experimental configurations in Fig. 1iii, a set of 2D and 3D cylindrical roughness elements were placed at 0.05c and 0.28c of each rotor blade to foster boundary layer transition. Where further downstream the boundary layer is expected to be thicker, resulting in the roughness element providing a smaller perturbation to the boundary layer. The 2D roughness consisted of a carefully glued 100 μ m wire and the 3D roughness was comprised of adhesive laser pre-cut cylindrical discrete roughness element spaced out at regular intervals, with a diameter of 1.27 mm, standard interval length of 2.54 mm and a of height of 200 μ m (commonly refereed to as "trip dots" or "CadCuts").

Table 1

Test matrix and associated motion blur, σ_{blur} , in IR images at $r/R = 0.7$.

Ω	f (Hz)	$Re_{r/R=0.3}(10^3)$	$Re_{r/R=1.0}(10^3)$	U_{tip} (m/s)	σ_{blur}
1000 RPM	17	6.2	22	13	0.03c
3000 RPM	50	19	66	39	0.08c
6500 RPM	108	40	144	85	0.17c

0.025./In total, one smooth and 8 roughness configurations at 6 different speeds where tested: the smooth rotor blade without any roughness is denoted as NoR, 2D roughness configurations are denoted as 2D and 3D roughness configurations are denoted as 3D2SR, 3D3SR, 3D4SR for roughness spanwise spacing of 5.04, 7.62 and 10.16 mm, respectively. At the end of the abbreviation either P1 or P2 is used to indicate the chordwise position of the roughness element, where P1 and P2 indicate 0.05c and 0.28c, respectively. The rotational speed, Ω , was varied from 1000 to 6500 RPM, yielding a Reynolds number range of 6.2×10^3 to 1.44×10^5 based on radial speed at the blade tip. The boundary layer thickness (δ) should be thicker for lower values of r/R and Re , and to understand the impact of the roughness element has on the flow, it is important to have the approximate value of δ over the rotor blade. In the following section the method for approximating the value of δ is presented.

2.2. Approximation of the boundary thickness

Due to the experimental difficulty in measuring the δ over a small-scale rotating surface, the boundary layer is approximated numerically. The purpose of estimating the boundary layer thickness was to compare it to the height of the roughness, and to estimate U_k the undisturbed velocity at the roughness height, to calculate the roughness Reynolds number, Re_k . The pressure over the surface of the rotor was calculated using XFOIL [27] for the local Reynolds number based on local radial speed and the effective aerodynamic angle of attack (α_{eff}) for the corresponding radial position and rotation speed was calculated using a Non Linear Vortex Lattice Method (NLVLM) which should take into account some of the 3D effects present, the method is explained in detail in Jo et al. [28]. Using the pressure obtained from XFOIL (calculated with an N-Factor of 7), the δ was calculated using ONERA's in house boundary layer code 3C3D, which solves Prandtl's boundary layer equations for three-dimensional boundary layers using a method of characteristics along local streamlines. To set up the boundary layer equations a body fitted coordinate system is used and the momentum equations are discretized along the local streamlines [29,30]. The results from 3C3D are presented in Table 2.

A frequently used criterion for determination of the critical roughness size for three-dimensional roughness was given by Von Doenhoff and Braslow [31] based on a limited body of experimental observations. In Von Doenhoff and Braslow [31], the roughness Reynolds number is introduced as, $Re_k = U_k k / \nu$, where k is the roughness height and U_k . By its nature, such a criterion, does not address the problem of shape and distribution of the roughness elements, however should suffice for the objectives of this current work. From Von Doenhoff and Braslow [31] the critical roughness Reynolds number for when a wedge forms is given as $Re_k \approx 600(d/k)^{-2/5}$, where d denotes the diameter of the roughness

Table 2

Estimation of the boundary layer thickness (δ) at chordwise positions of 0.05c and 0.28c and radial positions of $r/R = 0.3, 0.7$ and 0.95 . The α_{eff} was approximated to be $6.6^\circ, 4.6^\circ$ and 4.3° at $r/R = 0.3, 0.7$ and 0.95 , respectively for 1000 RPM, $4.0^\circ, 2.4^\circ$ and 2.0° for 3000 RPM and $2.2^\circ, 1.8^\circ$ and 1.9° for 6500. The δ is presented in mm. *For these configurations the boundary layer code does not compute further than 0.23c due to the formation of the laminar separation bubble. Therefore the δ is presented at 0.23c for both cases and should not change the conclusion of the results.

Ω	$r/R = 0.3$		$r/R = 0.7$		$r/R = 0.95$	
	$\delta_{0.05c}/k$	$\delta_{0.28c}/k$	$\delta_{0.05c}/k$	$\delta_{0.28c}/k$	$\delta_{0.05c}/k$	$\delta_{0.28c}/k$
1000 RPM	1.75	4.30*	1.15	3.05*	1.00	2.60
3000 RPM	1.00	3.05	0.55	1.40	0.50	1.45
6500 RPM	0.55	1.45	0.45	1.15	0.35	1.00

element. Using the boundary layer computations, the approximated range of Re_k for the current configuration is pretested in Fig. 2 with the critical roughness Reynolds number being $\sqrt{Re_k} \approx 17$. In addition to the criteria proposed by Von Doenhoff and Braslow [31], Gregory and Walker [32] conducted experiments using isolated roughness elements at various heights, both smaller and larger than δ . They found that at $\sqrt{Re_k} \approx 25$ a turbulent wedge would form directly behind the roughness element. Furthermore, they also studied roughness elements which were over 2δ and found that the turbulent wedge would increase in spanwise size near the roughness element, which is observed in the present work.

2.3. IR Thermography for detecting laminar to turbulent transition

The presumption of laminar to turbulent transition via IRT is based on the principle that laminar and turbulent flows have different heat transfer rates, where turbulent flows tend to have a higher rate of heat transfer between the bulk fluid flow and the blade surface, due to a higher value of skin friction, c_f . By means of the Reynolds assumption [22], the Stanton number illustrates this behavior and is defined in Eq. 2, where h denotes the heat transfer coefficient, ρ is the fluid density, U_∞ is the flow velocity and c_p is the pressure coefficient.

$$St = \frac{h}{\rho c_p U_\infty} \approx \frac{c_f}{2} \quad (2)$$

In this study, the grayscale pixel intensity of the images are used to quantify the flow instead of the temperature, due to the fact, that an accurate temperature calibration is fraught with difficulty because the temperature detected by the IR camera is dependent on the emitted heat from the surface of the model and of the reflected heat from the surroundings. As demonstrated by the Stanton number, the IR images reflect the characteristics of the flow field as a result of convection, the effect of conduction is considered to be negligible. The IR image pixel was normalized by the maximum pixel intensity present in the particular image so that the different test configurations could be more meaningfully compared. The normalised images showed little temporal variation in the flow topology, hence the time-averaged pixel intensity can be used to present the flow topology over the rotor. This metric was successfully used by [19,22,23] and here we denote it as I_n . For example, high and low levels of pixel intensity represent high and low temperatures, respectively. Richter and Schüllen [22] and Lang et al. [23] used chordwise pixel intensity profiles over the rotor blades to identify the

transition position, where the maximum pixel intensity ($\partial I_n / \partial x \approx 0$) is said to be the transition position, however care needs to be taken as the process of laminar to turbulent transition is one that occurs over a finite distance. The previous authors justified the use of this term by consistently referring to it as a physically significant location in the transition region. In the present work we do not use the maximum pixel intensity as a measure of transition location, rather as a marker to indicate that the flow could be separated or the friction being low due to low velocity fluid in a possibly separated flow. Hence, one could expect transition to occur around this region. Furthermore, it must be noted that one of the major limitations of the IRT technique is that it is a measurement of the heat signature of the boundary layer and not the actual boundary layer, resulting in some uncertainty when determining the transition location [22].

3. Results

3.1. Force and Torque Measurements

Thrust and torque measurements were conducted simultaneously with IR camera measurements. The coefficient of thrust and Figure of Merit (FM) and Power Loading (PL) are defined in Eq. (3)–(5), respectively. Where T is the thrust, Q is the torque, ρ is the density of the ambient air, Ω is the rotational frequency and R is the rotor blade radius. The objective of these measurements was not to find an optimal tripping configuration, rather to demonstrate that it is possible to measure the impact of the state of the boundary layer on a rotor operating at low Reynolds numbers.

$$C_T = \frac{T}{\frac{1}{2}\rho(\Omega R)^2 \pi R^2} \quad (3)$$

$$FM = \frac{T^{3/2}}{\Omega Q \sqrt{2\rho\pi R^2}} \quad (4)$$

$$PL = \frac{T}{\Omega Q} \quad (5)$$

Referring to Figs. 3 and 4., the FM and PL are presented. It is interesting to note that more tightly spaced roughness configurations perform worse than roughness configurations which were further apart. This signifies that the interaction and spreading of the wakes downstream of the

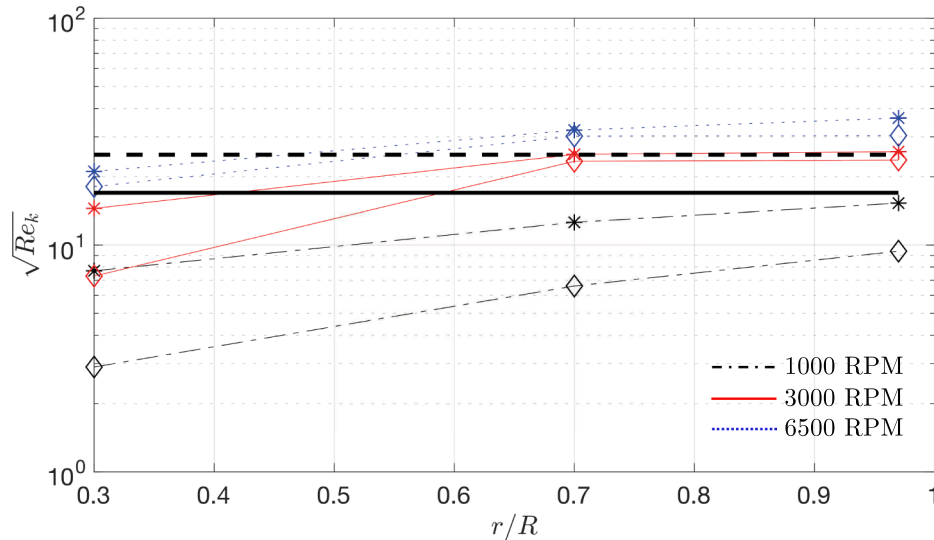


Fig. 2. The approximated range of $\sqrt{Re_k}$ for the current configuration at radial positions of $r/R = 0.3, 0.7$ and 0.95 for chordwise positions of $0.05c$ (*) and $0.28c$ (◇). The black horizontal line denotes the critical roughness Reynolds number, $\sqrt{Re_k} \approx 17$ [31] and the horizontal black dashed line denotes $\sqrt{Re_k} \approx 25$ proposed by [32].

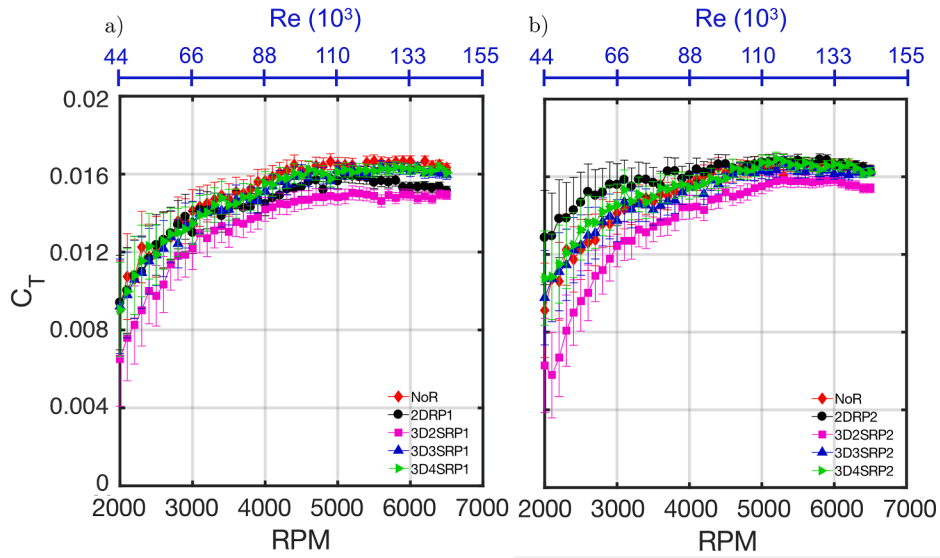


Fig. 3. Evolution of the coefficient of thrust with rotation speed for a) P1; b) P2 configurations. Error bars report the uncertainty for a 95% confidence interval.

roughness plays a significant role in the transition process and performance of the rotor. The present results show that at lower Reynolds numbers and RPM, the effects of roughness are more prominent and that forcing transition generally results in a decrease in performance both in terms of FM (Fig. 4.) and PL (Fig. 5), with a degradation of performance becoming more severe at higher RPM, up to approximately 25% in the the least favourable roughness configurations. However, at lower RPM, where the boundary layer is thicker there could be some modest performance improvements, as seen in the thrust for the 2DRP2 configuration (Fig. 3b.) and possibly in the FM and PL. The roughness height was not optimized in the present work, as a result there are regions on the rotor where the boundary layer that are "over tripped", resulting in massive performance loss, potentially due to increase in excrescence drag (also known as roughness drag, due to the imperfections of the aerodynamic surface such as surface discontinuities). Referring to Table 2, this is especially true at the higher RPM and Re, where $\delta \approx 1 - 2k$.

3.2. IR Measurements

3.2.1. Smooth Configuration

On a heated surface, IRT measurements would show that a separated region of flow cools down at rate much lower than for an attached flow. The same would be true for an LSB, the region of almost stationary or low velocity flow will undergo very slow temperature change compared to an attached laminar or turbulent flow with the rate of change in the latter being greater. A qualitative assessment of the temporal evolution of the normalised pixel intensity between suspected laminar and turbulent regions is presented in Fig. 6. To asses the differences between laminar and turbulent regions, the I_n (temperature higher with increasing I_n) was probed at six positions along the span of the rotor, with A,B and C located in a region where the flow is suspected to be turbulent and positions D, E and F in a possible laminar or separated region of flow. For positions A, B and C, the I_n decays rapidly due to high heat transfer between the flow and the blade surface, indicating more mixing and possibly a turbulent flow. Locations D, E and F could be in a region of low velocity, as the rate of change in temperature is lower and could correspond to lower velocities (such as in laminar separation or an

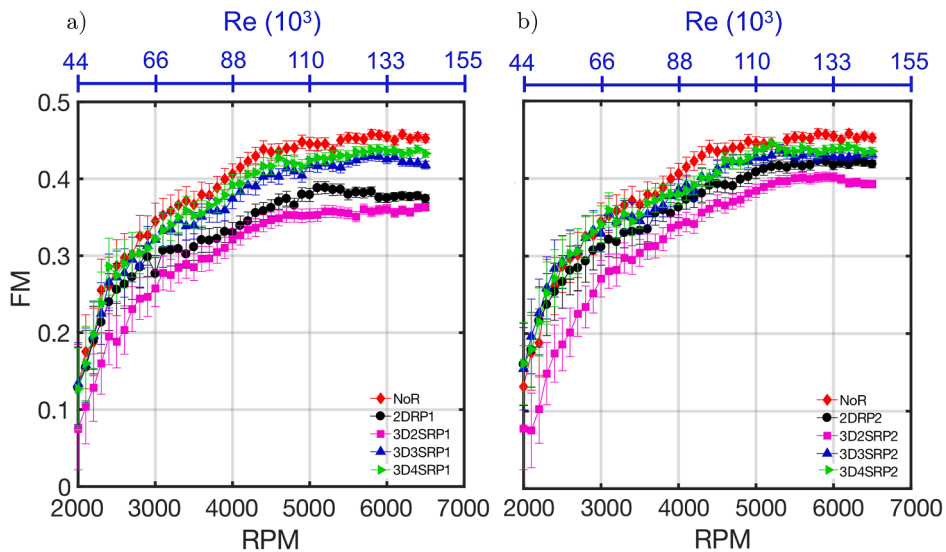


Fig. 4. Evolution of the figure of merit with rotation speed for a) P1; b) P2 configurations. Error bars report the uncertainty for a 95% confidence interval.

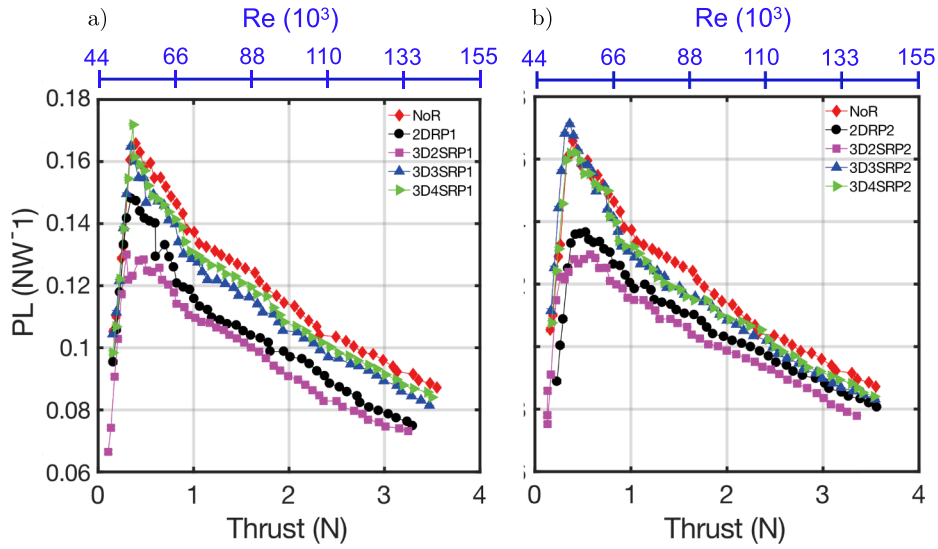


Fig. 5. Power loading curves for a) P1; b) P2 configurations.

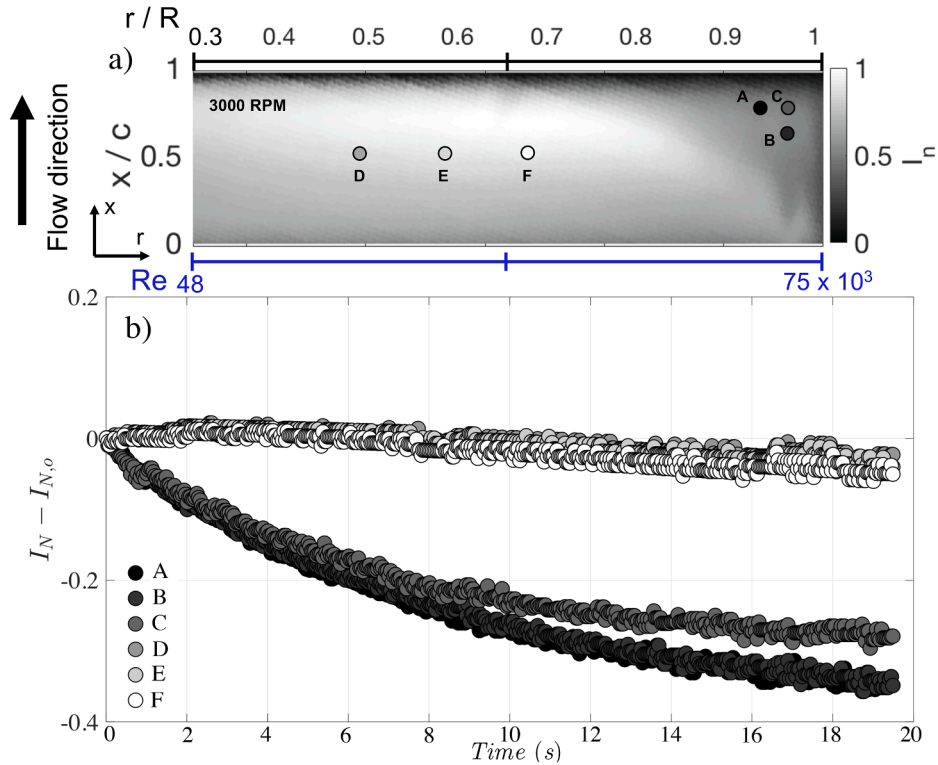


Fig. 6. a) IR measurements of NACA 0012 (NoR configuration) rotor at 3000 rpm; b) The differential temporal decay ($I_n - I_{n,0}$) of the normalized pixel intensity (cooling) in a region of relatively stagnant temperature (D,E,F) and a region of rapid decay (A,B,C). The time axis (x) is normalized by tip velocity (U_{tip}) and aerofoil chord (c).

LSB). Similar interpretations of IR data have been made by [19,20,24] to identify laminar, separated and turbulent regions of flow. Furthermore, experimental investigations with IRT and PIV measurements over a NACA0015 rotor by Lang et al. [23] and over a fixed aerofoil by [19], found IRT temperature signatures similar to those in the present work (Fig. 8) corresponded to LSBs. Whilst the low velocity regions (D, E and F) show similar behaviour in terms of rate of temperature change the flow is expected to behave rather differently from a laminar recirculating bubble over an unswept or 2D wing, where it retains spanwise uniformity. This is due to the fully 3D topology of flow as depicted in

Fig. 6b.

The time averaged IR measurements of the smooth, NoR configuration are presented in Fig. 7, for three different rotational speeds. The 3D nature of the flow is clearer, where the spanwise (radial) non-uniformity is accentuated with increasing rotational speed. Starting from the blade tip, the low levels of I_n could correspond to a turbulent flow or a possible tip vortex, even at low RPM, due to the high heat transfer rate between the blade surface and the higher energy flow. From Fig. 8 the rates of change in temperature along the chord in this region remains small due to the almost constant nature of the streamwise vorticity magnitude

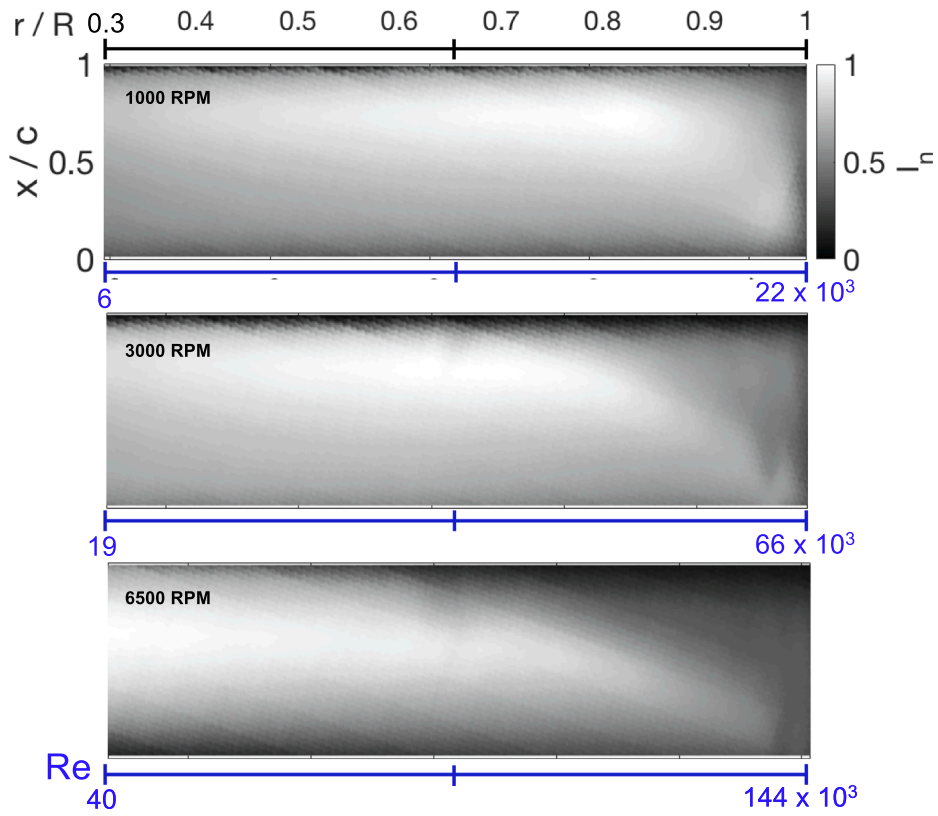


Fig. 7. IR measurements of NACA 0012 rotor for the Smooth (NoR) configuration.

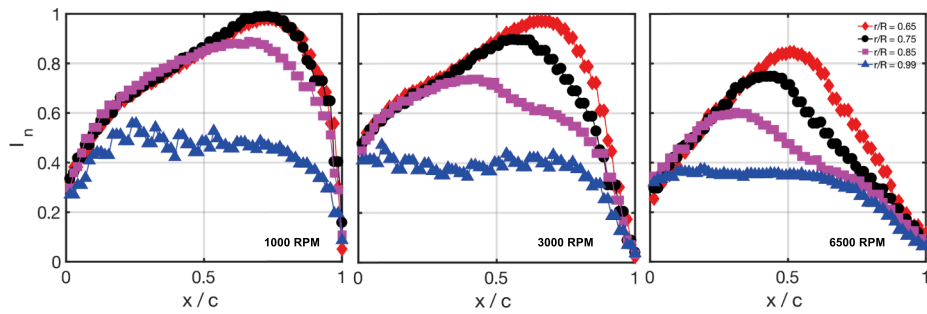


Fig. 8. Chordwise evolution of I_n for radial positions of $r/R = 0.65, 0.75, 0.85, 0.99$ for rotational speeds of 1000, 3000 and 6500 RPM for the Smooth (NoR) configuration.

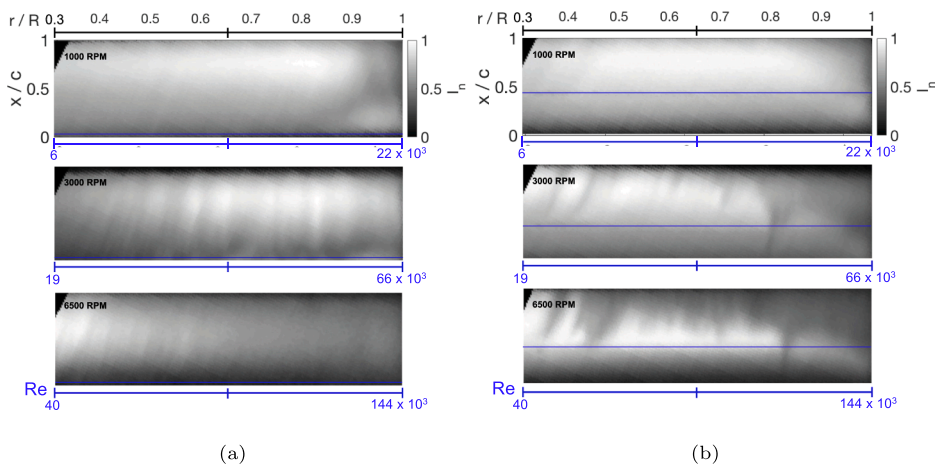


Fig. 9. IRT measurements of the 2D roughness configurations, where the blue line represents the tripping location. a) 2DRP1; b) 2DRP2.

along the turbulent flow or possible tip vortex, however from Fig. 7 the turbulent flow region propagates further inboard with increase in rotational speed.

The chordwise evolution of the pixel intensity is essentially the Stanton Number. A local quantitative assessment can be made from the chordwise profiles of I_n presented in Fig. 8, the maxima in pixel intensity indicates the region with low velocity similar to that in a separation bubble and rapid change in pixel intensity downstream would be due to high mixing turbulent flow. Therefore, here the location of maximum I_n , corresponds to the minimal value in skin friction and can be considered as occurring near the end of the transition process where further downstream turbulent reattachment could occur (if similarity was to be drawn with laminar separation bubble). The evolution of the pixel intensity to study transition has been adopted by [19,22,23].

3.2.2. 2D Roughness Configurations

The IR images of the 2D roughness configurations are presented in Fig. 9, with blue lines denoting the location of the $100\mu\text{m}$ wire. One of the major effects of the upstream 2D boundary layer trip is that the flow topology becomes more uniform in span (2D) compared to the untripped case, where a clear spanwisely varying (3D) flow topology was observed (refer to Fig. 7.). In the IR images, the low levels I_n should correspond to a turbulent flow. For the 2DRP1 configurations boundary layer transition appears to take place downstream of the wire as the Reynolds number is increased, which is expected as the boundary layer would be less stable. For the 2DRP2 configurations, an increase in the Reynolds number has the same effect, with the region of low pixel intensity moving closer to the wire. When the wire is at $0.28c$, the transition front moves further downstream of the wire, compared to when it is placed at $0.05c$. This is due to the fact that the boundary layer would be thicker at $0.28c$ than at $0.05c$ (refer to Table 2), therefore the wire could provide a smaller disturbance in the boundary layer. As the wire height increases with respect to δ the transition front will move upstream, closer to the wire. As for a 3D isolated roughness element (for example, refer to Fig. 2), there should be a critical roughness Reynolds number for which the flow will transition immediately downstream of the 2D wire. For radial positions where δ is close to the size of the wire, transition occurs rapidly downstream of the wire. For instance, in the 2DRP1 configurations, at 1000 RPM (where δ is $2-3\times$ the wire height) the flow remains relatively undisturbed compared to 6500 RPM (where δ is $0.7-1.1\times$ the wire height) where the flow appears to have been impacted by the presence of the wire and is possibly turbulent over most of the rotor blade (refer to Figs. 9a and b). The higher values of I_n behind the wire for 6500 RPM and partially for 3000 RPM in the 2DRP2 configuration (Fig. 9b) could be due to the wire causing the flow to separate, which would result in performance loss.

3.2.3. 3D Roughness Configurations

In this section, the results of boundary layer tripping via isolated cylindrical roughness elements are presented. Three roughness spacings at the same chordwise positions as in the 2D configurations were tested, making a total of six configurations. We observe the formation of turbulent wakes and wedges behind the roughness elements. The half-wedge angle, β is used to characterize a turbulent wedge which occurs once the wakes generated by the roughness elements have broken down or modal transition is bypassed where the wedge will form immediately downstream of the roughness. From the literature the value of β is typically between $5^\circ-10^\circ$ [33–35]. Turbulent wedges have been observed in many boundary layer transition problems for decades, yet the physical mechanism that drives spreading or even the value of β is not fully understood [33]. In the present work, the values of β were measured from the IR images and found to be between approximately $5^\circ-13^\circ$. Referring to Fig. 10, it can be observed that β increases with radial position and also at higher RPM. Beyond $r/R \approx 0.75$, the value β is larger than in previous studies [33–35] this could be due to the fact that δ is much smaller than the height of the isolated roughness element

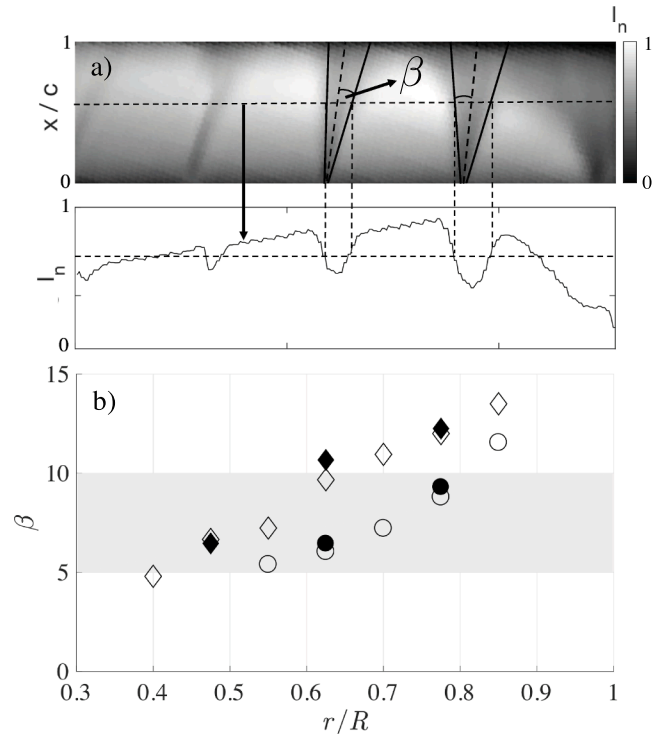


Fig. 10. a) Wedge half-angle (β) measurement from IR images; b) β where \diamond and \circ denote configurations at 6500 and 3000 RPM, respectively. Filled symbols denote the 3DR4S configuration and empty symbols denote the 3DR3S symbols. The grey band represents the range of β in the literature [33–35]. Configurations at 1000 RPM are not presented because wedges have did not form and the 3DR2S configurations are not presented because the turbulent wedges were to tightly spaced to make accurate measurements. The approximate uncertainty of the value of β is estimated to be 1° .

(Refer to Table 2).

Once the critical roughness Reynolds number is attained the streaks downstream of the isolated roughness break down into turbulent wedges as observed during very early experiments of Gregory and Walker [32]. At larger roughness Reynolds numbers the breakdown could occur immediately downstream of the roughness element, which is the case in the present work. Referring to Figs. 11–13, slight radial tilting of the wakes generated by the roughness elements is observed. The radial tilting appears to be largest near the root of the blade and decreases as r/R is increased. This point will be revisited in the discussion section.

In the majority of cases tested, turbulent wedges are observed right after the roughness element which is explained by the fact that the roughness elements are close to the size of the approximated boundary layer. From our measurements we observe that when the roughness Reynolds number, $\sqrt{Re_k} \approx 17-25$ turbulent wedges would develop, below this value the wakes generated by the roughness elements did not undergo break down. The results agree with previous work by [31,32], and demonstrate that the current experimental technique can be used for detecting transition over rotors applicable to MAS.

4. Discussion

The importance of modelling boundary layer transition reliably on rotor blades was demonstrated by Richez et al. [36] while trying to match their numerical simulation with experimental results. Here, from the force balance measurements when the boundary layer trip was introduced, overall deterioration in performance was observed in comparison to the smooth untripped rotor case, highlighting the importance of boundary layer transition on the performance of rotors. A similar effect was reported on scaled helicopter rotor blades at much higher

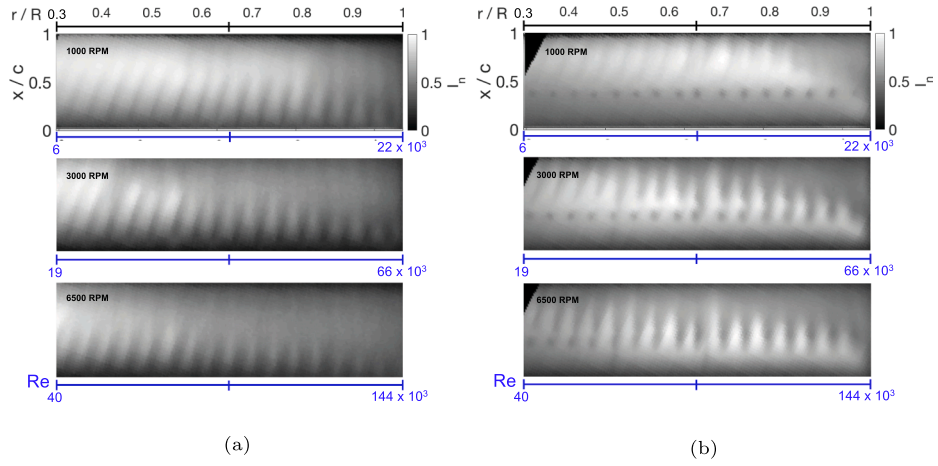


Fig. 11. IRT measurements of the 3D roughness high packing density configurations. a) 3DR2SP1;b) 3DR2SP2.

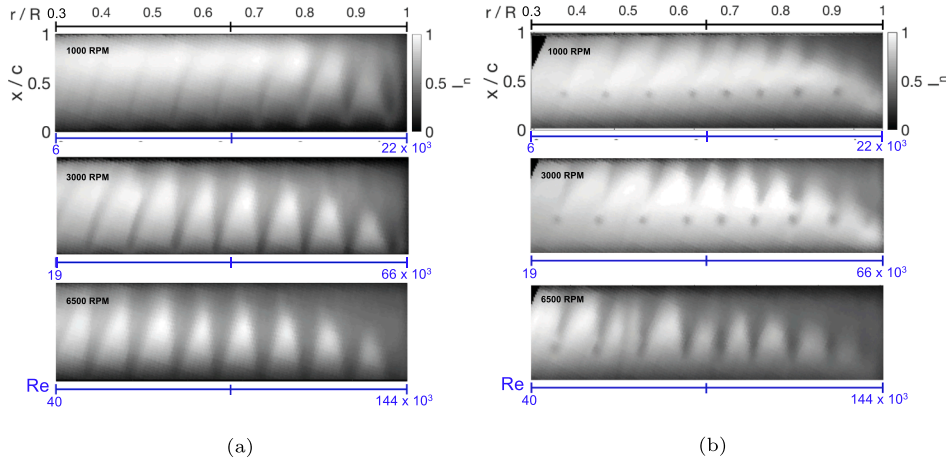


Fig. 12. IRT measurements of the 3D roughness medium packing density configurations. a) 3DR3SP1;b) 3DR3SP2.

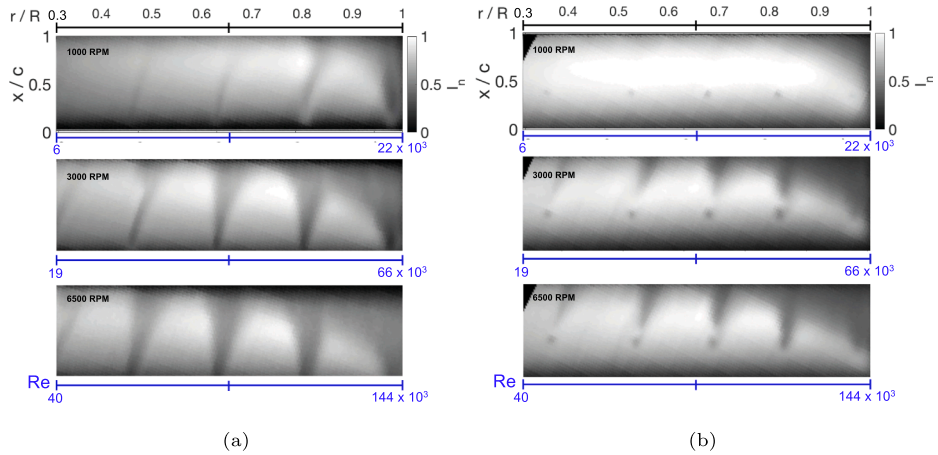


Fig. 13. IRT measurements of the 3D roughness low packing density configurations. a) 3DR4SP1; b) 3DR4SP2.

Reynolds numbers ($Re \sim 10^6$) by Overmeyer and Martin [37]. The effects of early transition on rotor performance is still not fully understood over a wide range of Reynolds numbers. For example, Jung and Baeder [38] conducted numerical simulations on a wind turbine rotor and found that forcing transition with optimal distributed surface roughness affects the performance differently depending on the state of the boundary layer. They found that in the presence of separated flows the

addition of upstream roughness could increase the performance up to 23.3% whereas it would result in a decrease of 8.3% for an attached flow. Recent numerical simulations on a rotor similar to the NASA Mars helicopter by Argus et al. [11] at $Re \leq 1 \times 10^5$, representative of the current experiment, showed that early transition caused by a decreased critical amplification factor resulted in a thrust increase through the elimination of laminar separation. At higher Re the benefit of early

transition diminished and became detrimental for the thrust produced by the rotor. They showed that the FM could be increased by 40% when the N-factor which is a measure of the growth rate of the perturbation in boundary layers (with lower value corresponding to higher growth rate) was reduced from 11 to 3. Here, improvement in the FM observed by Argus et al. [11] is not as straight forward, as early transition is fostered by roughness elements, which do not disrupt the flow in the same way as the variation of the critical amplification factor. Variation of the critical amplification factor changes the amount of perturbation growth in the boundary layer required for transition to occur whereas the addition of roughness elements adds a perturbation to the flow, and possibly bypassing the transition process all together. Since the current experiment was focused mainly on assessing the reliability of the IRT measurements for the characterisation of the topology of the flow on reduced size MAV rotors, no particular care was taken in identifying the optimal roughness size for boundary layer tripping to avoid excrescence drag which will act to degrade the performance of the rotor. In this case the torque which constitutes most of the drag will be more significantly affected as opposed to the thrust where lift plays a major contribution. Therefore, during the current investigation it was preferable to separate the analysis of the thrust characteristic from the torque, of course to the detriment of the FM which is a better representation of the overall performance. Performance improvement due to boundary layer tripping is more difficult to achieve in rotary wing configurations than in fixed wing configurations, due to the chord based Reynolds number being constant for the entire span of the fixed wing compared to the varying Reynolds number in the rotary configuration. Therefore, for a MAV rotor only a small section of the span of the blade could be in a Reynolds number regime that is appropriate for the boundary layer trip, in the other sections the trip could be detrimental to the performance.

Increasing the inter spacing between the 3D isolated roughness elements leads to a reduction in excrescence drag and increase in the FM due to a lesser number of roughness elements. Any benefits that the roughness could have (for example eliminating possible boundary separation) is thus counteracted by the higher drag. There could be an optimal ratio between roughness height and boundary layer thickness which would promote an increase in performance. For example optimal tripping could consist of varying the height of the roughness as a function of radial position, where the height of the trip would decrease as we approach the blade tip, since the boundary layer thickness becomes thinner with increasing radial position.

From Fig. 3b the effect of more efficient tripping can be observed through the increase in thrust at lower Reynolds number ($Re \leq 1 \times 10^5$) for the 2D roughness which performs better than the smooth case and all 3D roughness cases. At higher Reynolds numbers the thrust from the 2D roughness configurations starts to level-off with the smooth case indicating that in this regime a natural transition and reattachment might be taking place in some region of the smooth case itself. From a pure sectional analysis an efficient tripping of the boundary layer as confirmed from Fig. 9b would lead to an increase in sectional lift as the laminar separation region would be eliminated. The reduced zone of laminar separation region with increasing Reynolds number, a direct consequence of increasing RPM can be observed from Fig. 8. However, the increase in skin friction drag due to earlier transition from the 2D tripping would lead to an increase in total drag, thus reduction in FM as seen in Fig. 4. The trip wire also appeared to promote a more uniform transition whereas the 3D roughness resulted in localised effect and approached the 2D tripping condition with tighter spacing. However, since the 3D roughness height was higher this resulted in larger excrescence drag, again affecting torque, hence the FM, which was improved when the inter-roughness spacing and total number of discrete elements was reduced.

The sensitivity to the Reynolds number was clearer from the 3D roughness with the coarser spacing. In Fig. 13, for a moderate RPM of 3000 the development of the wake downstream of the roughness into fully turbulent wedges was accelerated in the outboard region of the

rotor blade due to the increase in the Reynolds number along the radial position. From early studies of Von Doenhoff and Braslow [31], an empirical correlation based on the height and diameter of the roughness element could predict when the turbulent wedge would form immediately after the roughness element, for the present roughness the critical roughness Reynolds number is $\sqrt{Re_k} \approx 17$. Gregory and Walker [32] demonstrated that for $\sqrt{Re_k} > 25$ immediate non-linear development into fully a turbulent wedge would take place instead of linear amplification of the wake, a transition mechanism usually referred to as ‘bypass’ in the literature. From Fig. 2, for RPM ≥ 3000 , in the region where $r/R \geq 0.7$ the roughness Reynolds number, $\sqrt{Re_k} > 17$ and therefore the rapid breakdown of the wakes into wedges in this region is in line with the criterion proposed in the literature. Furthermore, when the roughness height is above δ the turbulent wedge increases in spanwise size near the roughness element, which is what is observed in Gregory and Walker [32]. As demonstrated in Fig. 10, the size of the half-wedge angle, β agrees with previous literature when $r/R \leq 0.7$, [33–35]. Beyond $r/R = 0.7$, the values of β are slightly larger than in the literature and can be explained by the fact that the levels of motion blur are higher near the blade tip. Additionally, the higher values of β could also be due to a possible tip vortex contaminating the flow, this additional perturbation could increase the value of β . The mechanism of transition tripping from 3D roughness is significantly more complex and very recently Loiseau et al. [39] and Puckert and Rist [40] demonstrated using DNS and experiment, respectively, that it is through a global instability process, which is well beyond the scope of the current study. But, despite the highly 3D nature of the flow it is interesting to note that this semi-empirical criterion can still be used as an indicator for transition into fully developed wedges, an observation also made by Loiseau et al. [39].

Referring to Figs. 11–13, there appears to be slight radial tilting of the undeveloped wakes that could be caused by a spanwise flow over the rotor, which would be generated by the pressure gradient or rotational forces, or a combination of both. Lentnik and Dickinson [41] demonstrated that a dimensionless parameter used to quantify the relative contribution of the convective flow acceleration to Coriolis and centrifugal accelerations, the Rossby number, Ro , for a rotor blade with no approach velocity can be defined as $Ro = AR$. Therefore, for the current rotor, with $AR = 5$, the rotational forces should be of the same order of magnitude as the convective forces. Weiss et al. [42] found that when the local $AR = 4.76$, there are no effects of rotational forces on the boundary layer transition or chordwise extent of laminar flow over a DSA-9A aerofoil rotor. Further numerical simulations by Hernandez [43] over a NACA0015 rotor showed that rotational forces can have a stabilising effect on boundary transition when Ro tended towards 1. These encourages further investigation of rotational effects on boundary layer transition and suggest that the traditional sectional analysis coupled with blade element momentum theory might not be sufficient to explain the transition process and therefore their reliability for low Reynolds number rotor design and optimisation should be verified.

5. Conclusion

The feasibility of conducting an experiment that allows the assessment of the effect of boundary layer transition on a reduced size and low Reynolds number rotor has been demonstrated. The rotation of the rotor imposes serious constraints with regards to detailed characterisation of the flow, but here we have demonstrated that coupled force balance and phase-locked IR-thermography measurements can help in gaining more insight into the flow topology and states which can have an impact on performance. The effect of boundary layer transition or suppression of a laminar separation at low Reynolds number, on the performance of the rotor is confirmed on a highly simplified configuration and therefore this accentuates the importance of transition modelling during the design and optimisation of low Reynolds number rotors. Tripping the boundary

layer or suppression of the laminar separation can also have an effect on aeroacoustic or aeroelastic performance; therefore further investigation will be encouraged. Even if in this specific case a general decrease in performance was observed due to early transition, some indications of a positive effect on performance are present. Therefore, further investigation should be conducted on the effects the state the boundary layer has on MAV rotor performance, for example, profile optimisation, elimination of boundary layer separation, optimized boundary layer trips which limit the amount of excrescence drag, different rotor configurations and the impact of freestream turbulence on the boundary layer transition mechanisms. The complex fully 3D flow topology and radial curling of the undeveloped wakes from the 3D roughness suggests that there is strong spanwise flow due to the interactions between the rotational accelerations and streamwise and radial pressure gradients. Therefore, this calls for further understanding of the effect of rotational forces or Rossby number on the transition mechanism to improve transition prediction and optimisation of low Reynolds number rotors.

Declaration of Competing Interest

The authors declare that they have no known competing financial interests or personal relationships that could have appeared to influence the work reported in this paper.

Acknowledgements

We thank Remy Chanton and Henri Dedieu for their technical support during the experimental program, Sylvain Belliot for fabricating the rotor model, Olivier Cherrier for the Infrared Camera and Pietro Li Volsi for assisting in the NLVLM calculations.

References

- [1] S. Watkins, M. Thompson, B. Loxton, M. Abdulrahim, On low altitude flight through the atmospheric boundary layer, *International Journal of Micro Air Vehicles* 2 (2) (2010) 55–68.
- [2] A. Watkins, M. Thompson, M. Shortis, R. Segal, M. Abdulrahim, J. Sheridan, An overview of experiments on the dynamic sensitivity of MAVs to turbulence, *The Aeronautical Journal* 114 (1158) (2010) 485–492.
- [3] M. Gaster, The structure and behaviour of laminar separation bubbles, NPL (1967).
- [4] C. Haggmark, A.A. Bakchinov, P.H. Alfredsson, Experiments on a two-dimensional laminar separation bubble, *Philosophical Transactions of the Royal Society of London, Series A: Mathematical, Physical and Engineering Sciences* 358 (1777) (2000) 3193–3205.
- [5] O. Marxen, M. Lang, U. Rist, S. Wagner, A combined experimental/numerical study of unsteady phenomena in a laminar separation bubble, *Flow, Turbulence and Combustion* 71 (1–4) (2003) 133–146.
- [6] S. Hosseinverdi, H.F. Fasel, Numerical investigation of laminar–turbulent transition in laminar separation bubbles: the effect of free-stream turbulence, *J. Fluid Mech.* 858 (2019) 714–759.
- [7] H. Xu, S.M. Mughal, E.R. Gowree, C.J. Atkin, S.J. Sherwin, Destabilisation and modification of Tollmien–Schlichting disturbances by a three-dimensional surface indentation, *J. Fluid Mech.* 819 (2017) 592–620.
- [8] B. Carmichael, Low Reynolds number airfoil survey, volume 1, NASA 165803 1.
- [9] P. Lissaman, Low-Reynolds-number airfoils, *Annual review of fluid mechanics* 15 (1) (1983) 223–239.
- [10] R.K. Singh, M.R. Ahmed, Blade design and performance testing of a small wind turbine rotor for low wind speed applications, *Renewable Energy* 50 (2013) 812–819.
- [11] F.J. Argus, G.A. Ament, W.J. Koning, The influence of laminar-turbulent transition on rotor performance at low Reynolds numbers, VFS Technical Meeting on Aeromechanics for Advanced Vertical Flight, San Jose, CA, January 21–23, 2020.
- [12] C.C. Wolf, A.D. Gardner, M. Raffel, Infrared thermography for boundary layer transition measurements, *Meas. Sci. Technol.* 31 (11) (2020) 112002.
- [13] B. Chanetz, J. Détery, P. Gilliéron, P. Gnemmi, E.R. Gowree, P. Perrier, *Experimental Aerodynamics*, Springer, 2020.
- [14] K. Horstmann, A. Quast, G. Redeker, Flight and wind-tunnel investigations on boundary-layer transition, *Journal of Aircraft* 27 (2) (1990) 146–150.
- [15] C. Dollinger, M. Sorg, N. Balaesque, A. Fischer, Measurement uncertainty of infrared thermographic flow visualization measurements for transition detection on wind turbines in operation, *Exp. Thermal Fluid Sci.* 97 (2018) 279–289.
- [16] A. Séraudie, J. Perraud, F. Moens, Transition measurement and analysis on a swept wing in high lift configuration, *Aerospace science and technology* 7 (8) (2003) 569–576.
- [17] M. Raffel, C.B. Merz, Differential infrared thermography for unsteady boundary-layer transition measurements, *AIAA journal* 52 (9) (2014) 2090–2093.
- [18] A. Weiss, C.C. Wolf, K. Kaufmann, J.N. Braukmann, J.T. Heineck, M. Raffel, Unsteady boundary-layer transition measurements and computations on a rotating blade under cyclic pitch conditions, *Exp. Fluids* 61 (2) (2020) 61.
- [19] M. Miozzi, A. Capone, M. Costantini, L. Fratto, C. Klein, F. Di Felice, Skin friction and coherent structures within a laminar separation bubble, *Exp. Fluids* 60 (1) (2019) 13.
- [20] D.W. Wynnchuk, S. Yarusevych, Characterization of laminar separation bubbles using infrared thermography, *AIAA Journal* 58 (7) (2020) 2831–2843.
- [21] V. Maldonado, S. Gupta, Increasing the power efficiency of rotors at transitional Reynolds numbers with synthetic jet actuators, *Exp. Thermal Fluid Sci.* 105 (2019) 356–366.
- [22] K. Richter, E. Schüle, Boundary-layer transition measurements on hovering helicopter rotors by infrared thermography, *Experiments in fluids* 55 (7) (2014) 1755.
- [23] W. Lang, A. Gardner, S. Mariappan, C. Klein, M. Raffel, Boundary-layer transition on a rotor blade measured by temperature-sensitive paint, thermal imaging and image derotation, *Exp. Fluids* 56 (6) (2015) 118.
- [24] R. Thiessen, E. Schüle, Infrared thermography and dit of quadcopter rotor blades using laser heating, in: *Multidisciplinary Digital Publishing Institute Proceedings*, Vol. 27, 2019, p. 31.
- [25] P. Schäfer, J. Severin, H. Herwig, The effect of heat transfer on the stability of laminar boundary layers, *International journal of heat and mass transfer* 38 (10) (1995) 1855–1863.
- [26] T. Desert, J. Moschetta, H. Bezard, Aerodynamic design of a martian micro air vehicle, in: *Proceedings of the 7th European Conference for Aeronautics and Aerospace Sciences*, 2017.
- [27] M. Dreha, Xfoil: An analysis and design system for low Reynolds number airfoils, in: *Low Reynolds number aerodynamics*, Springer, 1989, pp. 1–12.
- [28] Y. Jo, T. Jardin, R. Gojon, M.C. Jacob, J.-M. Moschetta, Prediction of noise from low Reynolds number rotors with different number of blades using a non-linear vortex lattice method, in: *25th AIAA/CEAS Aeroacoustics Conference*, 2019, p. 2615.
- [29] R. Houdeville, Three-dimensional boundary layer calculation by a characteristic method, in: *Fifth Symposium on Numerical and Physical Aspects of Aerodynamic Flows*, Long Beach, January 1992, 1992.
- [30] J. Perraud, O. Vermeersch, R. Houdeville, Descriptif et mode d'emploi du code 3c3d, ONERA, RT 1 (2011) 18325.
- [31] A.E. Von Doenhoff, A.L. Braslow, The effect of distributed surface roughness on laminar flow, in: *Boundary layer and flow control*, Elsevier, 1961, pp. 657–681.
- [32] N. Gregory, W. Walker, The effect on transition of isolated surface excrescences in the boundary layer, HM Stationery Office (1956).
- [33] D. Goldstein, J. Chu, G. Brown, Lateral spreading mechanism of a turbulent spot and a turbulent wedge, *Flow, Turbulence and Combustion* 98 (1) (2017) 21–35.
- [34] J. Watmuff, Evolution of a turbulent wedge from a streamwise streak, in: *Proc. 15th Australian Fluid Mech. Conf.*, Sydney, Australia, 2004.
- [35] S. Zhong, T. Chong, H. Hodson, A comparison of spreading angles of turbulent wedges in velocity and thermal boundary layers, *J. Fluids Eng.* 125 (2) (2003) 267–274.
- [36] F. Richez, A. Nazarians, C. Lienard, Assessment of laminar-turbulent transition modeling methods for the prediction of helicopter rotor performance, in: *rd European Rotorcraft Forum*, 2017.
- [37] A.D. Overmeyer, P.B. Martin, Measured boundary layer transition and rotor hover performance at model scale, in: *55th AIAA Aerospace Sciences Meeting*, 2017, p. 1872.
- [38] Y.S. Jung, J. Baeder, Simulations for effect of surface roughness on wind turbine aerodynamic performance, in: *Journal of Physics: Conference Series*, Vol. 1452, IOP Publishing, 2020, p. 012055.
- [39] J.-C. Loiseau, J.-C. Robinet, S. Cherubini, E. Leriche, Investigation of the roughness-induced transition: global stability analyses and direct numerical simulations, *Journal of Fluid Mechanics*.
- [40] D.K. Puckert, U. Rist, Global instability in a laminar boundary layer perturbed by an isolated roughness element, *Exp. Fluids* 59 (3) (2018) 1–6.
- [41] D. Lentink, M.H. Dickinson, Biofluiddynamic scaling of flapping, spinning and translating fins and wings, *J. Exp. Biol.* 212 (16) (2009) 2691–2704.
- [42] A. Weiss, A.D. Gardner, T. Schwermer, C. Klein, M. Raffel, On the effect of rotational forces on rotor blade boundary-layer transition, *AIAA Journal* 57 (1) (2019) 252–266.
- [43] G.G.M. Hernandez, Laminar-turbulent transition on wind turbines, Technical University of Copenhagen, Denmark Phd Thesis.